CHAPTER 3

Result and Discussion

3.1 Characterization

The hydrothermal method was used to synthesis CMC-$AgInS_2$ QDs. In contrast to the conventional organic phase synthetic method, this method is simple, cost-effective, environmentally friendly and allows for biocompatibility. In our hydrothermal method synthesis of CMC-$AgInS_2$ QDs, ternary $AgInS_2$ QDs were initially produced by the reaction of silver nitrate and indium nitrate with sulfur sources ($Na_2S_2O_3 \cdot 5H_2O$, $C_3H_7NO_2S$ and C_2H_5NS) in the presence of CMC was coated onto the surface of $AgInS_2$ QDs to form CMC-$AgInS_2$ QDs at 200 °C for 2 and 24 h. As shown in Table 3.1, Rod-, sheet-, plate- and sphere $AgInS_2$ QDs can be obtained through the change of the concentration of silver nitrate or the sulfur source.

Table 3.1 Shape of the synthesis CMC-$AgInS_2$ QDs by hydrothermal method.

Sample	$AgNO_3$ (mmol)	Sulfur source	Temperature (°C)	Time (h)	Shape
1	1	C_2H_5NS	200	2	-
2	2	C_2H_5NS	200	2	-
3	3	C_2H_5NS	200	2	-
4	1	C_2H_5NS	200	24	rods
5	2	C_2H_5NS	200	24	sheets
6	3	C_2H_5NS	200	24	plates
7	1	$Na_2S_2O_3 \cdot 5H_2O$	200	24	-
8	1	$C_3H_7NO_2S$	200	24	spheres

The influence of concentration of silver nitrate and sulfur sources ($Na_2S_2O_3 \cdot 5H_2O$, $C_3H_7NO_2S$ and C_2H_5NS) on different shapes of the CMC-$AgInS_2$ QDs was investigated.

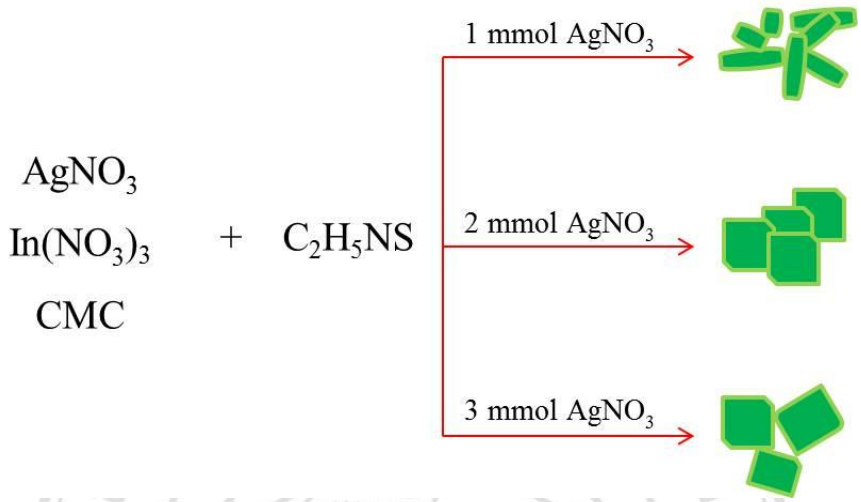

Figure 3.1 Schematic diagram of synthesis of CMC-$AgInS_2$ QDs with different of concentration of silver nitrate.

When CMC-$AgInS_2$ QDs has been carried out by using C_2H_5NS as a sulfur source, silver nitrate of different concentrations (1, 2 and 3 mmol) as precursors and the lengths of reaction time of 24 h, the products were nanorods, nanosheets and nanoplates, respectively. The higher precursor concentrations are in favor the growth of planar nanocrystals [8]. These results were in consistence with the previous report [8, 50].

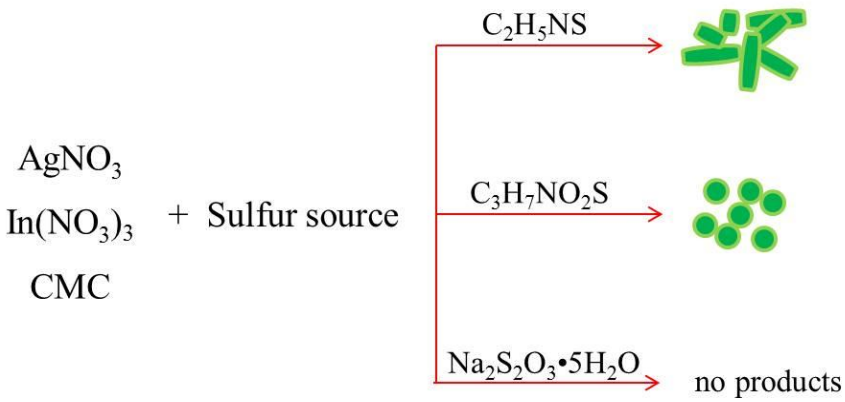

Figure 3.2 Schematic diagram of synthesis of CMC-$AgInS_2$ QDs with different of sulfur source.

When C_2H_5NS was used as the sulfur source, the release rate of sulfur was very rapid comparing with those for using $C_3H_7NO_2S$ and $Na_2S_2O_3 \cdot 5H_2O$ as sulfur sources. The product was well-defined nanorods (sample 4). Upon changing the sulfur source from C_2H_5NS to $C_3H_7NO_2S$, the release rate of sulfur was slowdown. Generally, there are two critical factors responsible for the shape of nanocrystals. One is the nucleation process and the other is the subsequent growth stage [8]. The rate of nucleation and growth became optimum and the spherical nanoparticles (sample 8) with small size of about 10 nm were synthesized. When $Na_2S_2O_3 \cdot 5H_2O$ was employed as the sulfur source, the release rate of sulfur would be extremely slow and no products were synthesized. Therefore the synthesis of CMC-$AgInS_2$ QDs was used $C_3H_7NO_2S$ of sulfur source with appropriate nanocrystals wherewith $C_3H_7NO_2S$ is an inexpensive, simple, and environment-friendly thiol-containing amino acid, which serves as both of sulfur source and template in the formation of metal sulfide nanostructures [16].

From the synthesis and the modification of surface and functionalization of $AgInS_2$ QDs to from CMC-$AgInS_2$ QDs, which can be categorized into growing QDs within polymeric template (growing inside) [51] as shown in Figure 3.3.

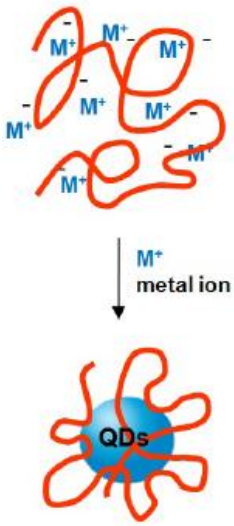

Figure 3.3 Schematic synthesis of growing QDs within polymeric template [51].

This method used polymer (carboxymethyl cellulose sodium salt) and metal ion from silver nitrate, indium nitrate and sodium thiosulfate pentahydrate or L-cystein or thioacetamide. The metal ions are then chemically transformed *via* reduction or precipitation reactions into $AgInS_2$ QDs. Through this method, $AgInS_2$ QDs can be grown inside polymer and polymer acts as the protective shell for $AgInS_2$QDs in aqueous solution [51].

3.1.1 Transmission electron microscope (TEM)

Figure 3.4 TEM images of CMC-$AgInS_2$ QDs synthesized by hydrothermal method (sample 4).

The morphology and nanostructure of the CMC-$AgInS_2$ QDs were observed by using a transmission electron microscope (TEM) operated at 200 kV. Figure 3.4 shows the TEM images of CMC-$AgInS_2$ QDs using C_2H_5NS as a sulfur source and 1 mmol of silver nitrate as precursors. From the TEM images, we can see that rods-shape of product. The product was well-defined nanorods (sample 4) with the width (diameter) of 15 to 30 nm and the length ranging from 60 to 170 nm. These results were in consistence with the previous report [8].

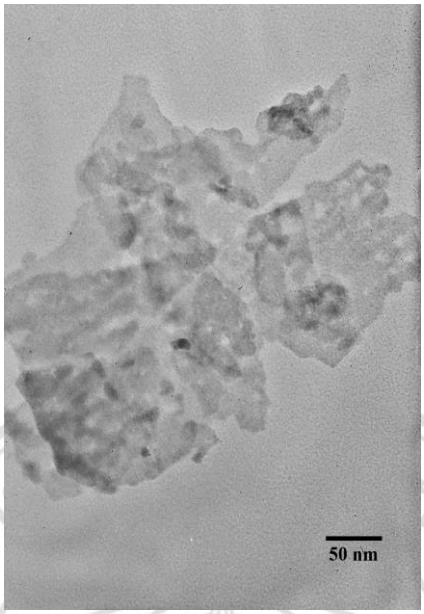

Figure 3.5 TEM images of CMC-$AgInS_2$ QDs synthesized by hydrothermal method (sample 5).

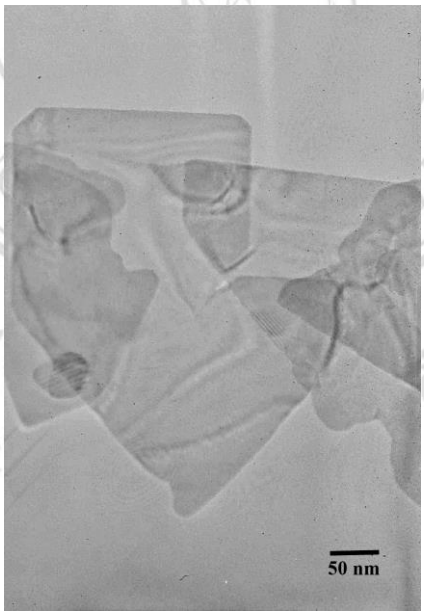

Figure 3.6 TEM images of CMC-$AgInS_2$ QDs synthesized by hydrothermal method (sample 6).

The TEM images of CMC-$AgInS_2$ QDs using C_2H_5NS as a sulfur source and 2 and 3 mmol of silver nitrate as precursors shown in Figure 3.5 and 3.6. The product was well-defined nanosheets (sample 5) and nanoplates (sample 6).

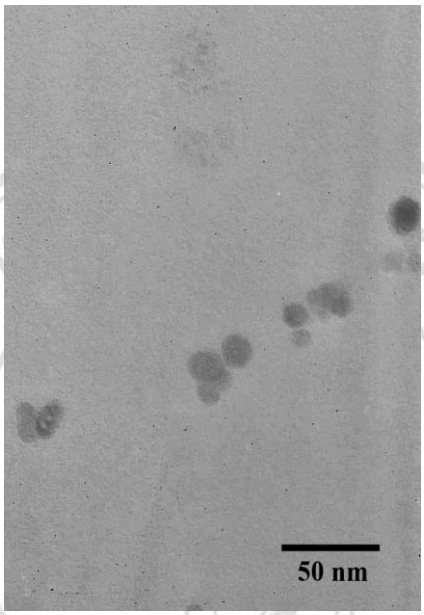

Figure 3.7 TEM images of CMC-$AgInS_2$ QDs synthesized by hydrothermal method (sample 8).

Figure 3.7 shows TEM image of CMC-$AgInS_2$ QDs was used $C_3H_7NO_2S$ of sulfur source. The average of silver indium sulfide nanocrystals size was 10 nm. The products were composed nanorods, nanosheets, nanoplates and nanospheres in the shapes.

3.1.2 X-ray diffractometer (XRD)

The phase and purity of CMC-$AgInS_2$ QDs were studied by using an X-diffractometer. The XRD patterns of CMC-$AgInS_2$ QDs was identified *via* the Joint Committee on Powder Diffraction Standards (JCPDS) file no. 25-1328 [49].

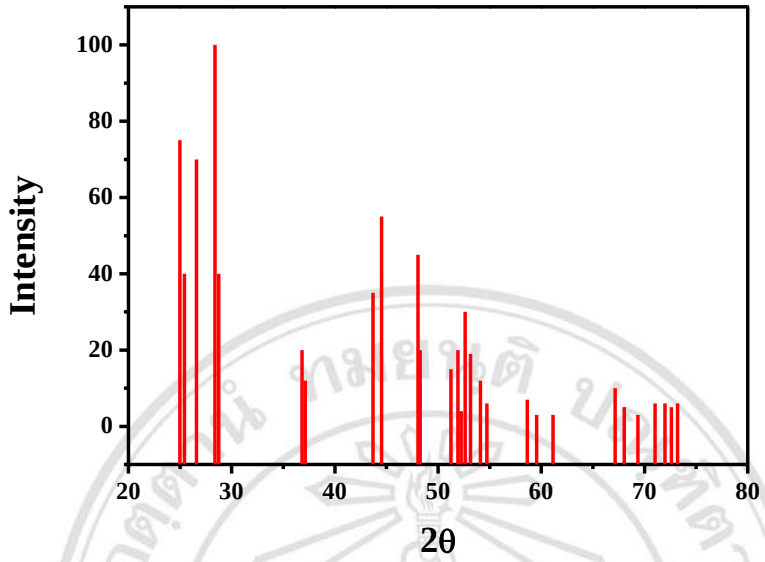

Figure 3.8 XRD patterns of $AgInS_2$ (JCPDS 25-1328).

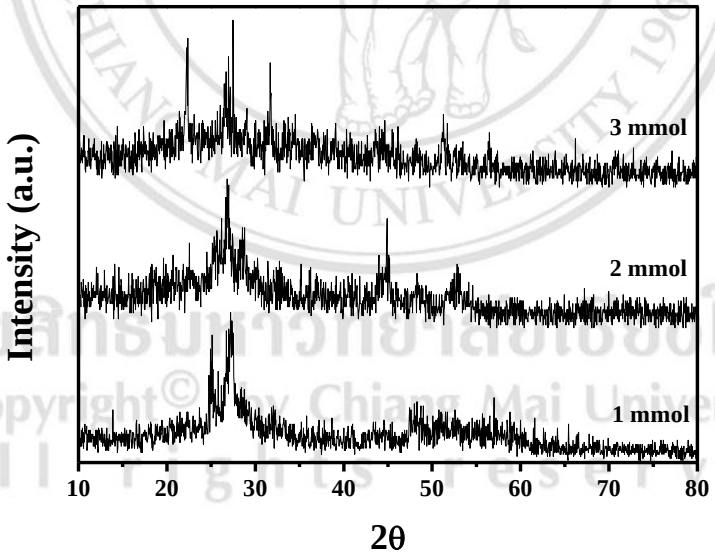

Figure 3.9 XRD patterns of CMC-$AgInS_2$ QDs synthesized by hydrothermal method: sample 4, sample 5 and sample 6.

Figure 3.9 shows XRD patterns of CMC-$AgInS_2$ QDs synthesized by hydrothermal method (sample 4, sample 5 and sample 6). That result was compared and it corresponded to the JCPDS no.25-1328 [49]. The CMC-$AgInS_2$ QDs were assigned to (120), (200), (002), (121), (201), (040), (320), (123) and (322) planes, respectively, of the single orthorhombic structure of $AgInS_2$ crystal, no other characteristic peaks of impurities were observed.

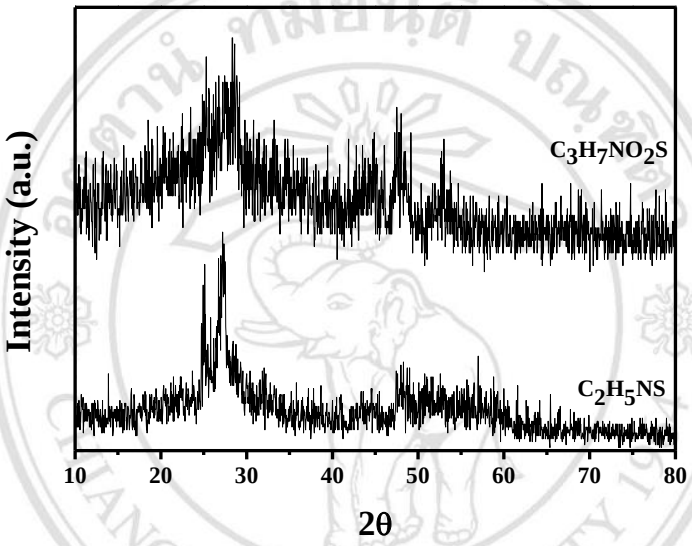

Figure 3.10 XRD patterns of CMC-$AgInS_2$ QDs synthesized by hydrothermal method: sample 4 and sample 8.

The XRD pattern shown in Figure 3.10, CMC-$AgInS_2$ QDs synthesized by hydrothermal method (sample 4 and sample 8). The diffraction peaks agree with the orthorhombic $AgInS_2$. Because of the size of the sample are small, the XRD spectrum of the samples are broad peak [52].

As we all know, the orthorhombic $AgInS_2$ is a high-temperature phase which is stable above 620 °C, while the low-temperature phase, tetragonal $AgInS_2$ is stable below 620 °C. However, in this present work, we have obtained the metastable orthorhombic $AgInS_2$ nanocrystals at even 200 °C. The reason might be that the solvent as water and pressure of reaction has

changed the chemical growth environment, leading to the phase reversion temporarily [8].

3.1.3 X-ray photoelectron spectroscope (XPS)

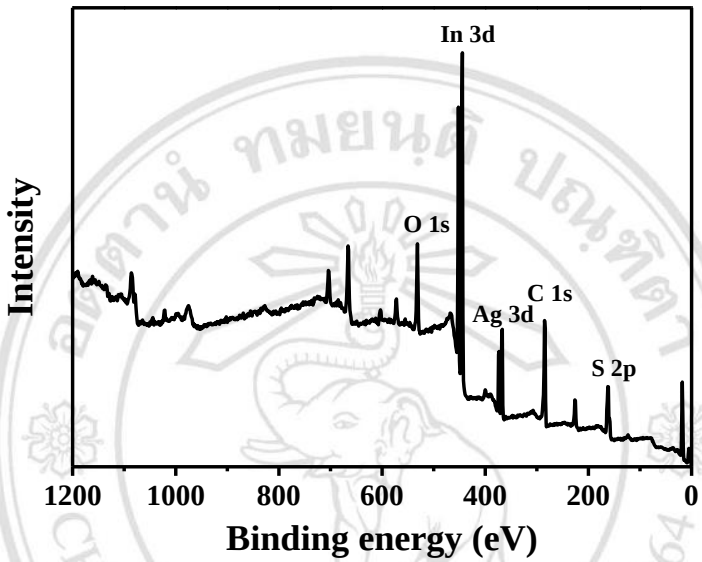

Figure 3.11 XPS spectra of the CMC-$AgInS_2$ QDs synthesized by hydrothermal method: survey.

The surface chemical composition and element valence state of materials characteristics by using XPS. Figure 3.11 shows the survey spectrum, the main peaks belonged to Ag, In, S, C, and O elements.

From Figure 3.12 – 3.16, it can be seen that Ag 3d peaks, In 3d peaks, S 2p peaks, C 1s peaks and O 1s peaks.

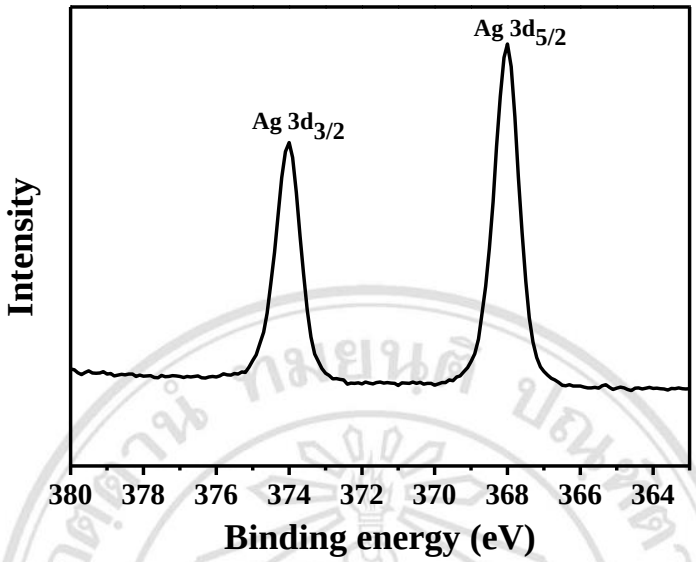

Figure 3.12 XPS spectra of the CMC-$AgInS_2$ QDs synthesized by hydrothermal method: Ag 3d.

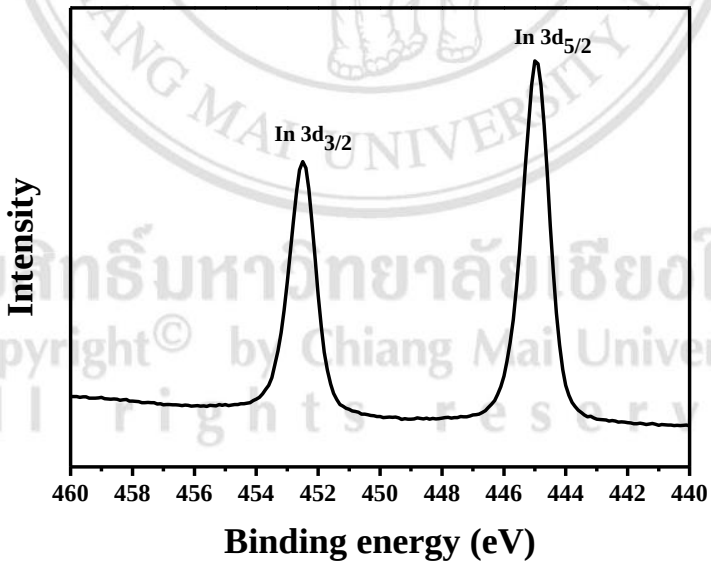

Figure 3.13 XPS spectra of the CMC-$AgInS_2$ QDs synthesized by hydrothermal method: In 3d.

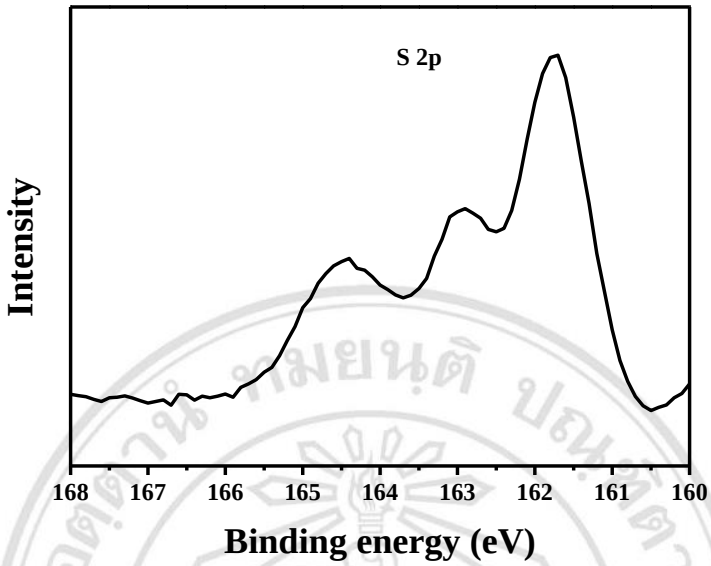

Figure 3.14 XPS spectra of the CMC-$AgInS_2$ QDs synthesized by hydrothermal method: S 2p.

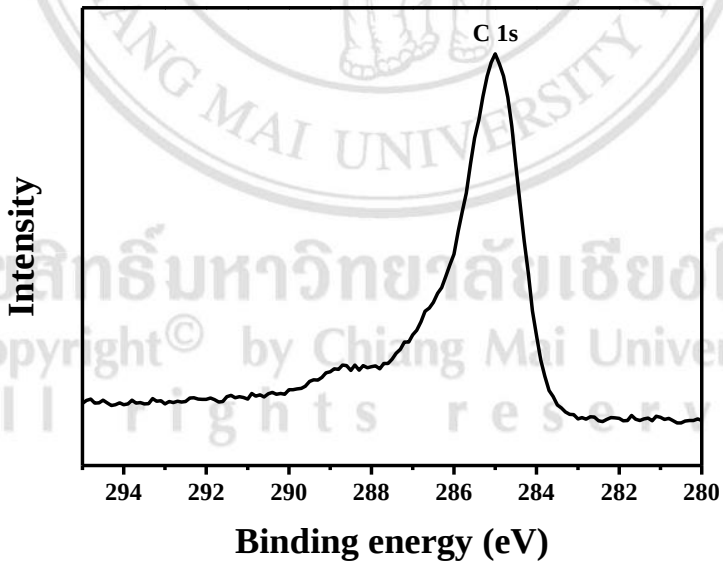

Figure 3.15 XPS spectra of the CMC-$AgInS_2$ QDs synthesized by hydrothermal method: C 1s.

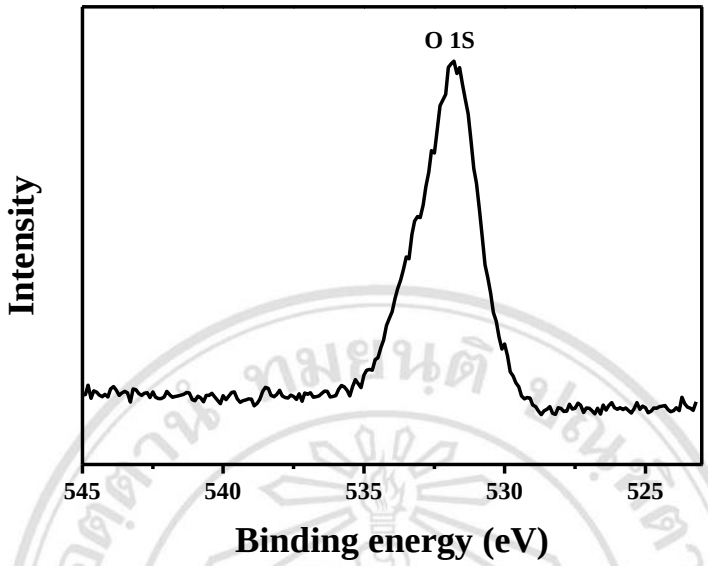

Figure 3.16 XPS spectra of the CMC-$AgInS_2$ QDs synthesized by hydrothermal method: O 1s.

These results showed that the chemical states of element composed the CMC-$AgInS_2$ QDs were Ag^+, In^{3+}, S^{2-}, C and O. Therefore, the results of XPS measurements illuminated that the product was the CMC-$AgInS_2$ QDs. The element chemical composition was a good agreement with the previous report [14, 16, 53, 54].

3.1.4 Dynamic light scattering (DLS)

The hydrodynamic size characteristics by using DLS. All measurements were carried out at 25 °C. The range of hydrodynamic size of the CMC-$AgInS_2$ QDs synthesized by hydrothermal was 200 – 300 nm.

Table 3.2 Hydrodynamic size of the CMC-$AgInS_2$ QDs synthesized by hydrothermal method.

Sample	Hydrodynamic size (nm)	Standard Deviation
4	285.80	23.28
5	232.48	30.04
6	243.72	48.85
8	193.94	14.65

The hydrodynamic diameter will depend not only on the size of the particle "core", but also on any surface structure. The range of hydrodynamic size of the CMC-$AgInS_2$ QDs more than size of the CMC-$AgInS_2$ QDs from TEM because of effect of ionic strength, surface structure and non-spherical particles. They should be noted that the Malvern Zetasizer analyzer was done on the CMC-$AgInS_2$ QDs dispersed in the aqueous solution (wet state). But for the TEM analysis, it was done on the CMC-$AgInS_2$ QDs which were in the dried state. Thus the hydrodynamic size determined by the Malvern Zetasizer Nano-S was larger than the particle size characterized by TEM. The CMC-$AgInS_2$ QDs dispersed in the solution (wet QDs) were looser than those in the dried state (dried QDs).

3.1.5 Fourier transform infrared spectrometer (FTIR)

The functional groups of the CMC-$AgInS_2$ QDs was studied by using FTIR with KBr. The FTIR spectrum of pure CMC is presented in Figure 3.17. Vibration peaks at around 3400 cm^{-1} attributed to the stretching vibration of O-H stretching. Vibration peaks at around 1609 cm^{-1} and 1408 cm^{-1} are attributed to the stretching vibration of COO^- stretching. Vibration peaks at around 1062 cm^{-1} is attributed to the stretching vibration of C-O stretching [20, 22].

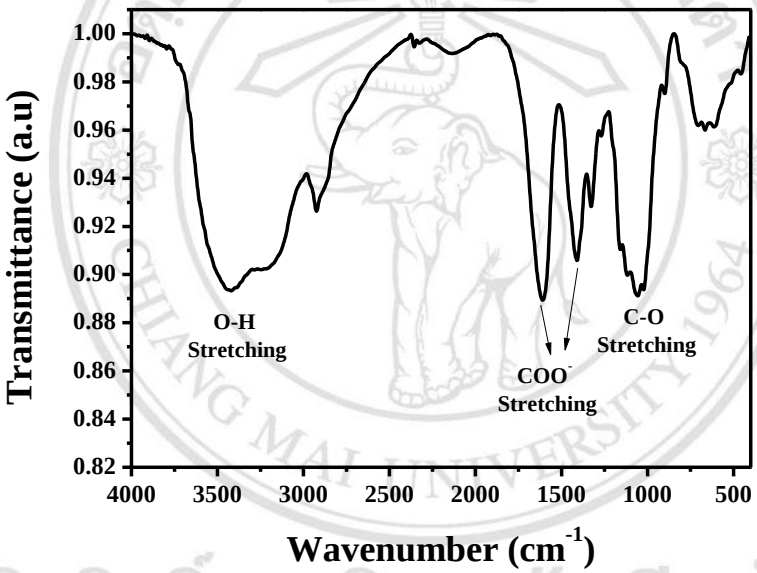

Figure 3.17 FTIR spectrum of CMC.

The FTIR spectrum of CMC-$AgInS_2$ QDs synthesized by hydrothermal method are presented in Figure 3.18-3.21.

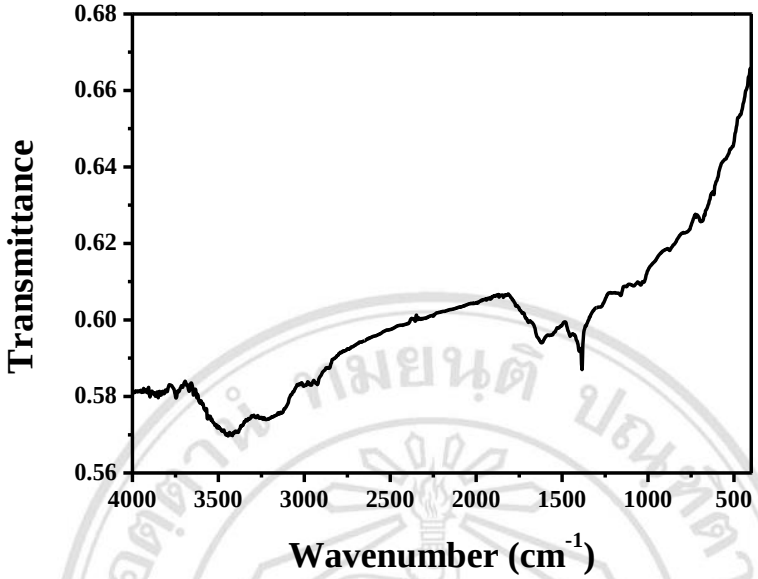

Figure 3.18 FTIR spectrum of CMC-$AgInS_2$ QDs synthesized by hydrothermal method (sample 4).

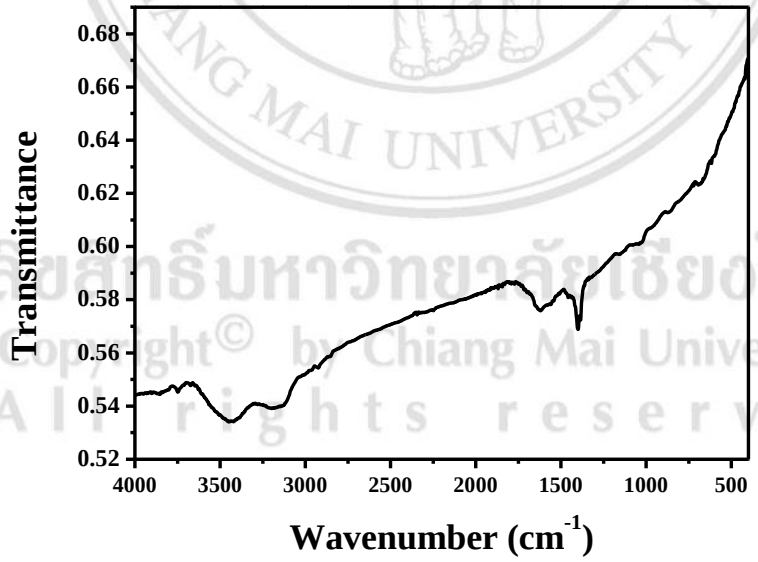

Figure 3.19 FTIR spectrum of CMC-$AgInS_2$ QDs synthesized by hydrothermal method (sample 5).

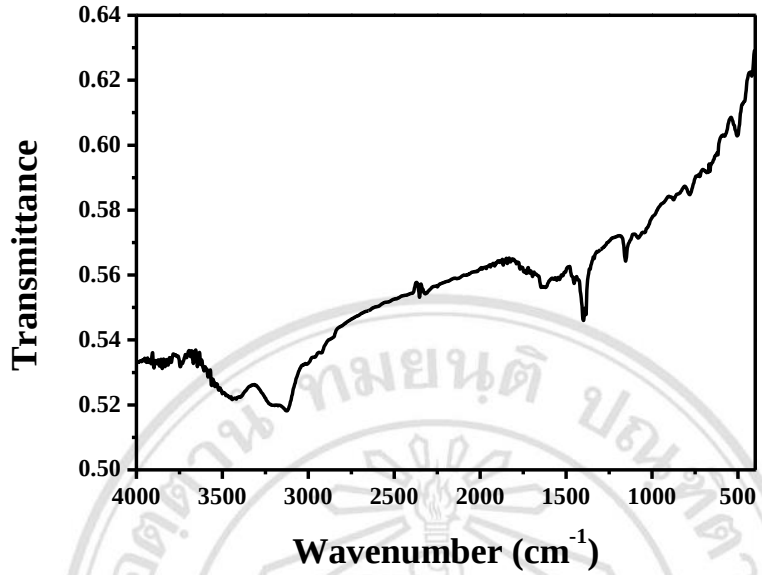

Figure 3.20 FTIR spectrum of CMC-$AgInS_2$ QDs synthesized by hydrothermal method (sample 6).

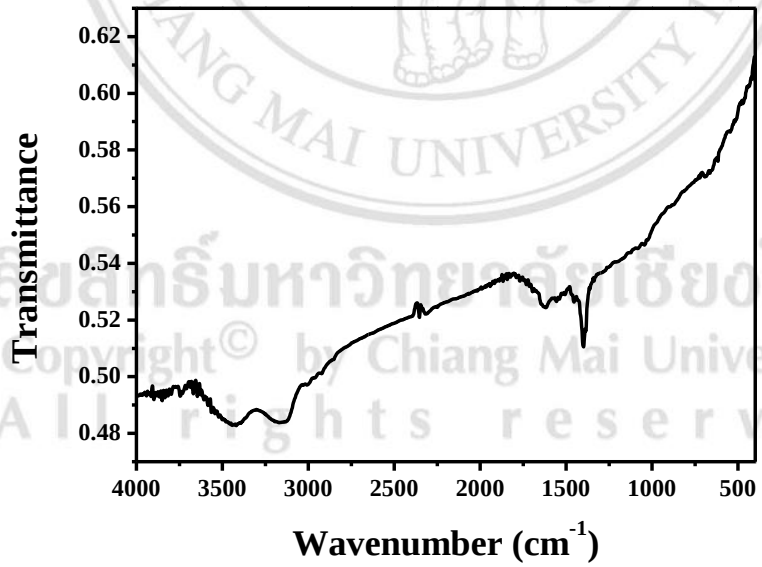

Figure 3.21 FTIR spectrum of CMC-$AgInS_2$ QDs synthesized by hydrothermal method (sample 8).

The functional groups of the CMC-$AgInS_2$ QDs synthesized by hydrothermal method were characterized by FTIR and the results are shown in Figure 3.22 and 3.23.

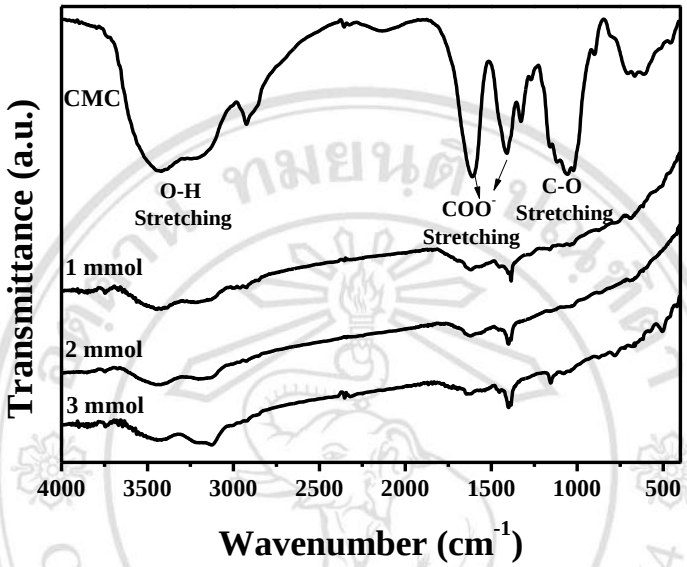

Figure 3.22 FTIR spectra of CMC-$AgInS_2$ QDs synthesized by hydrothermal method: sample 4, 5 and 6.

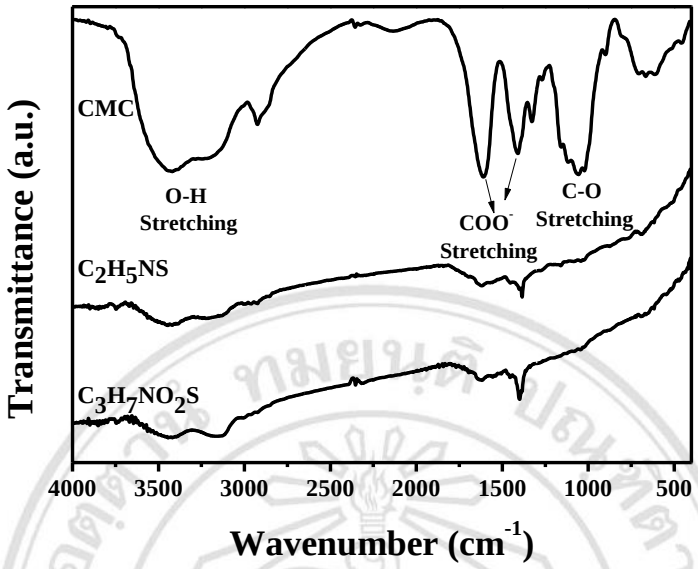

Figure 3.23 FTIR spectra of CMC-$AgInS_2$ QDs synthesized by hydrothermal method: sample 4 and 8.

Vibration peaks at around 3400 cm^{-1} attributed to the stretching vibration of O-H stretching and vibration peaks at around 1609 cm^{-1} and 1408 cm^{-1} are attributed to the stretching vibration of COO^- stretching indicating the presence of the CMC molecules on the CMC-$AgInS_2$ QDs. These results were in consistence with the previous report [20, 22].

3.1.6 Thermogravimetric analyzer (TGA)

Thermal analysis was performed using TGA. The TGA curve of $AgInS_2$ as shown in Figure 3.24.

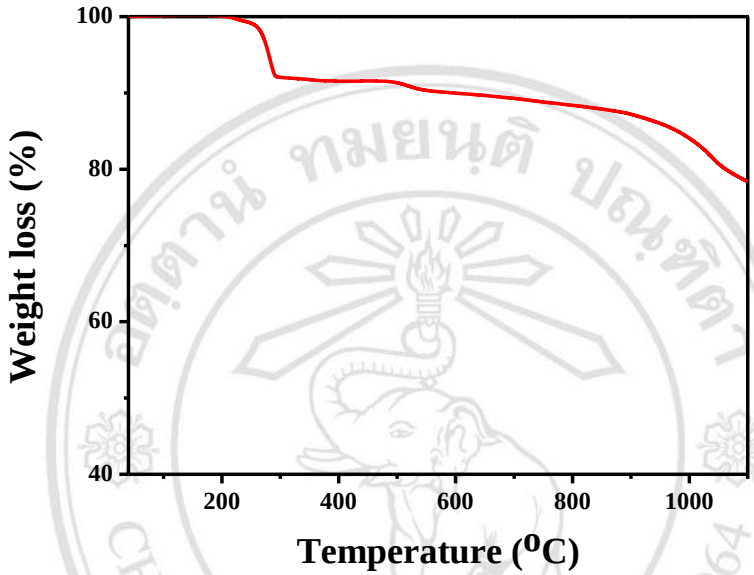

Figure 3.24 TGA curve of $AgInS_2$.

For $AgInS_2$ QDs, the transformation of the $AgInS_2$ QDs was completed at a temperature of about 213 °C. Thus, these results confirm that CMC was successfully coated onto the surface of $AgInS_2$ QDs by using a hydrothermal synthesis.

The TGA curve of CMC-$AgInS_2$ QDs synthesized by hydrothermal method are presented in Figure 3.25-3.27.

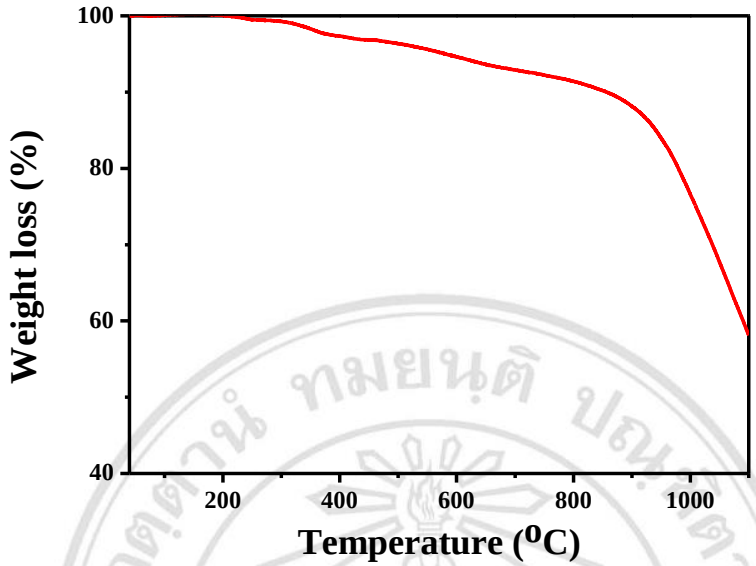

Figure 3.25 TGA curve of CMC-$AgInS_2$ QDs synthesized by hydrothermal method (sample 5).

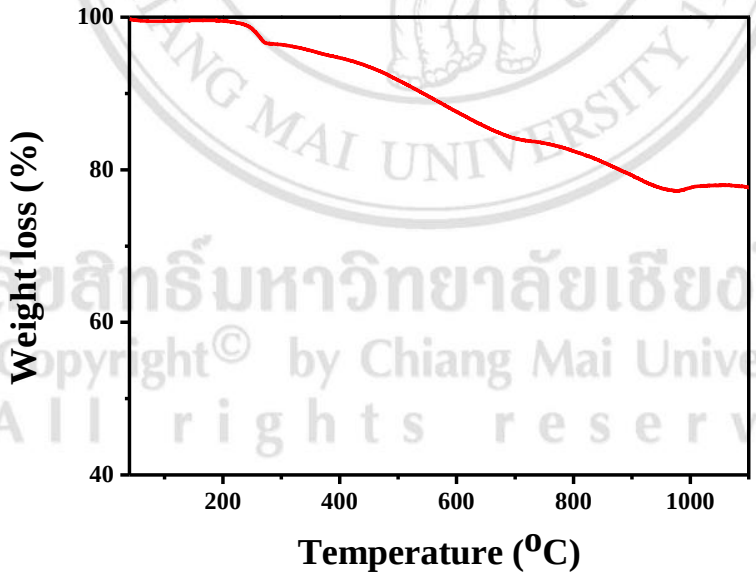

Figure 3.26 TGA curve of CMC-$AgInS_2$QDs synthesized by hydrothermal method (sample 6).

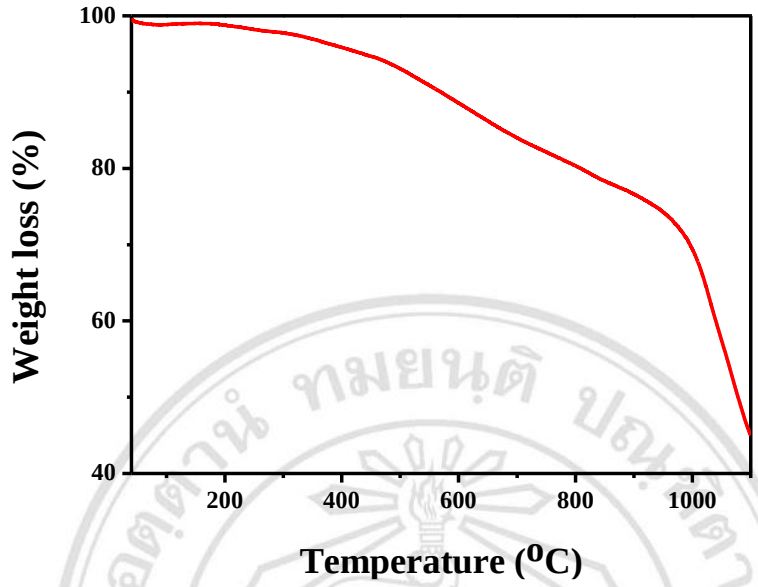

Figure 3.27 TGA curve of CMC-$AgInS_2$ QDs synthesized by hydrothermal method (sample 8).

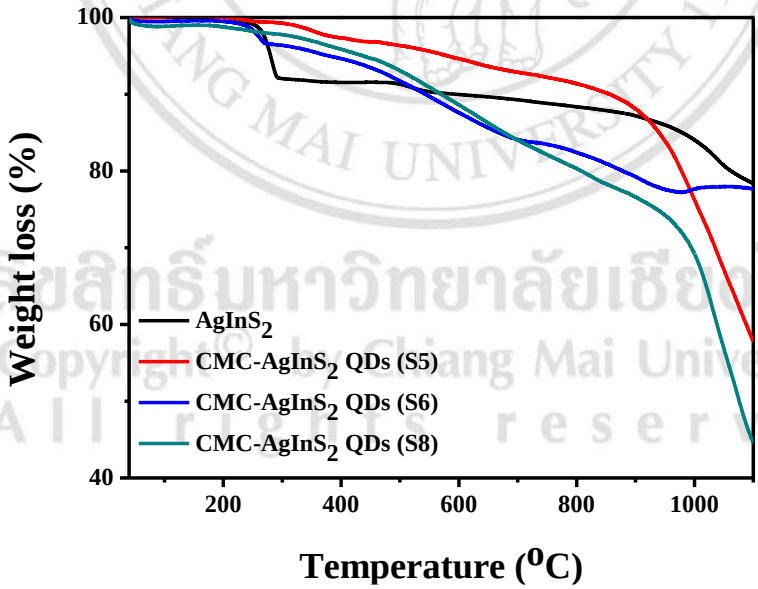

Figure 3.28 TGA curve of $AgInS_2$ and CMC-$AgInS_2$ QDs synthesized by hydrothermal method.

In the TGA curves of CMC, the weight loss in CMC-$AgInS_2$ QDs increases with decomposition step indicating that with the increase of temperature, the weight loss is very significant. An initial weight loss at 50 – 200 °C is due to the evaporation of the different types of absorbed water molecules. Above this range is the weight loss which was attributed to the loss of CO_2 from the polysaccharide. The decomposition of carboxymethyl cellulose displayed around 250 °C [22]. The weight loss at 500 – 750 °C is loss of excess volatile sulfur react with oxygen to from sulfur dioxide gas and escaping from the compound. The weight loss at about 1,000 °C is the solid state phase transition of the $AgInS_2$ into Ag and Ag_2S crystal phase [55, 56].

As shown in Figure 3.28, The COO^- groups of CMC could be decarboxylated in this temperature range. Due to the present analysis, that the percentage of CMC on CMC-$AgInS_2$ QDs as sample 5, sample 6 and sample 8 are approximately 3, 5 and 5%, respectively.

The crystals displayed thermal stability up to 600 °C. The TGA curve of composite displayed a similar pattern that of raw carboxymethyl cellulose indicating the decomposition of carboxymethyl cellulose around 250 °C. The sharp drop in weight in the second area that is observed in the curve of carboxymethyl cellulose was absent in the curve of nanocrystals indicating the presence of $AgInS_2$ QDs in the nanocrystals. From the results it is evident that nanocrystals was composed of carboxymethyl cellulose and $AgInS_2$ QDs. These results was a good agreement with the previous report [22].

3.1.7 UV-Vis spectrophotometer

The optical properties of CMC-$AgInS_2$ QDs study by UV-Vis spectrophotometer over the wavelength range from 200 to 800 nm and photoluminescence spectrometer at room temperature. The qualitative analysis of CMC-$AgInS_2$ QDs was initially investigated by a UV-visible spectrophotometer.

The energy gap was calculated from absorption spectra by extrapolating to the Tauc relation [57]:

$$(\alpha h\nu)^2 = B(h\nu - E_g)$$

where α = absorbance of photon energy
$h\nu$ = photon energy
B = a constant
E_g = the energy gap

The linear portion of the absorption slope $(\alpha h\nu)^2$ vs $h\nu$ is the energy gap of the sample.

The measured band gap energy of CMC-$AgInS_2$ QDs synthesized by hydrothermal method (sample 4) was found to be 3.98 eV as shown in Figure 3.29.

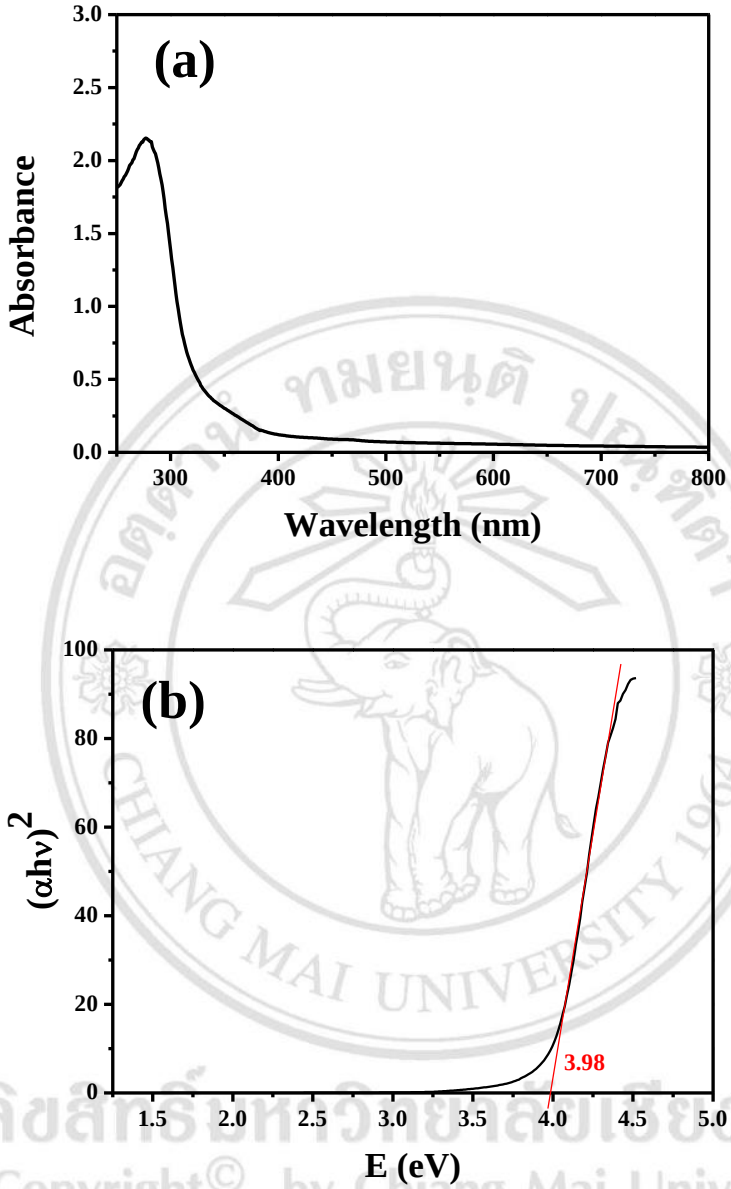

Figure 3.29 Absorbance spectra and band gap energy of CMC-$AgInS_2$ QDs synthesized by hydrothermal method (sample 4).

The measured band gap energy of CMC-$AgInS_2$ QDs synthesized by hydrothermal method (sample 5) was found to be 3.92 eV as shown in Figure 3.30.

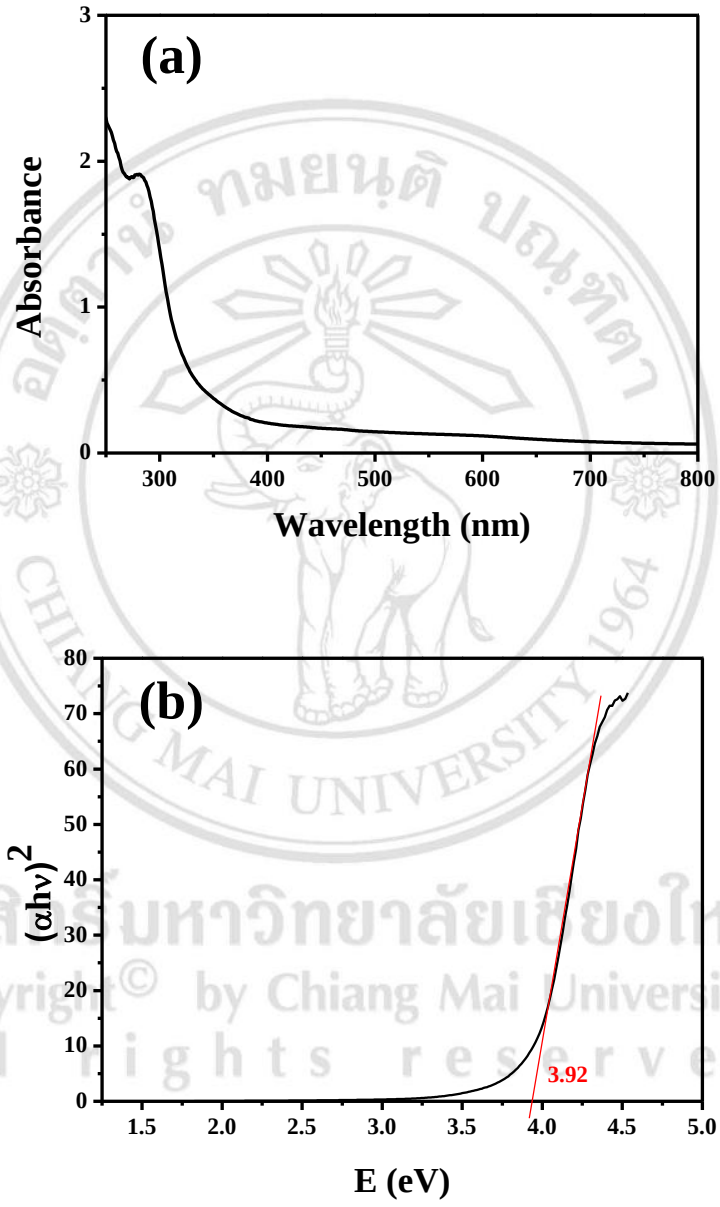

Figure 3.30 Absorbance spectra and band gap energy of CMC-$AgInS_2$ QDs synthesized by hydrothermal method (sample 5).

The measured band gap energy of CMC-$AgInS_2$ QDs synthesized by hydrothermal method (sample 6) was found to be 3.93 eV as shown in Figure 3.31.

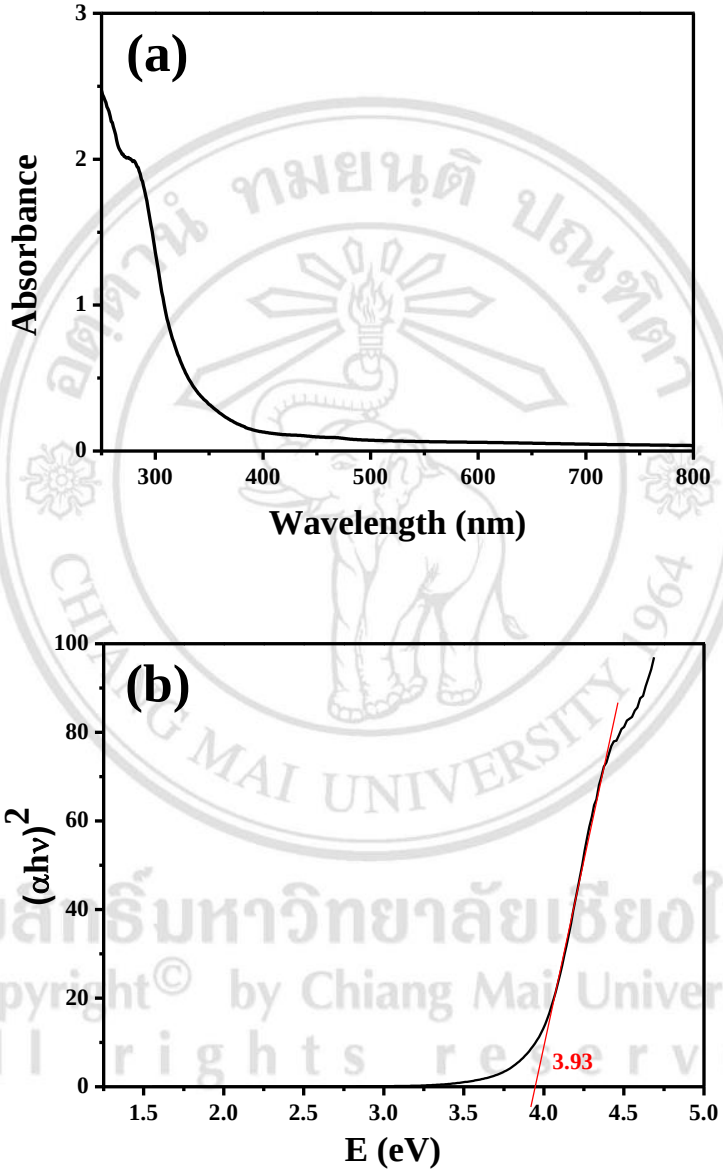

Figure 3.31 Absorbance spectra and band gap energy of CMC-$AgInS_2$ QDs synthesized by hydrothermal method (sample 6).

The measured band gap energy of CMC-$AgInS_2$ QDs synthesized by hydrothermal method (sample 8) was found to be 3.92 eV as shown in Figure 3.32.

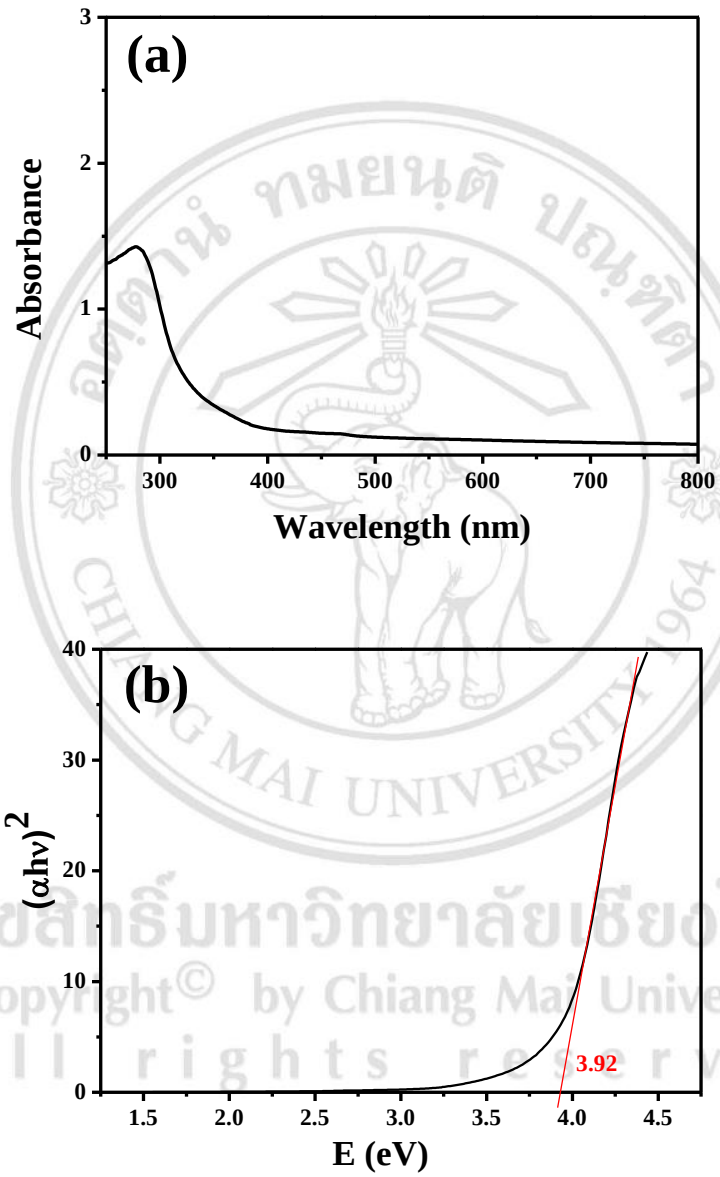

Figure 3.32 Absorbance spectra and band gap energy of CMC-$AgInS_2$ QDs synthesized by hydrothermal method (sample 8).

Compared with the band gap of GSH-$AgInS_2$ nanocrystals at 3.48 ± 0.01 eV [9] our prepared CMC-$AgInS_2$ QDs have band gap energy from 3.92 to 3.98 eV. The largest value reported to date because of difference condition reaction and the slightly reduced quantum confinement [9, 57].

3.1.8 Photoluminescence spectrometer

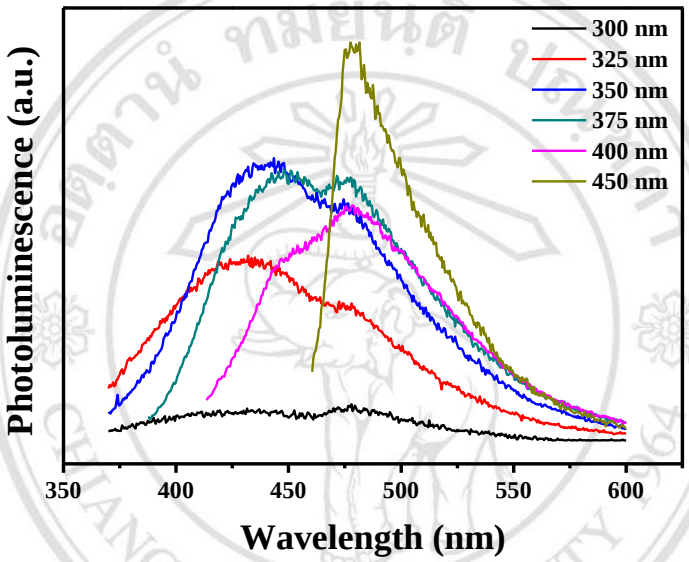

Figure 3.33 Photoluminescence spectra of CMC-$AgInS_2$ QDs synthesized by hydrothermal method excited from 300 – 450 nm.

As shown in Figure 3.33, the maximum emission wavelength was shifted from 430 nm to 480 nm as the excitation wavelength was varied from 300 – 450 nm.

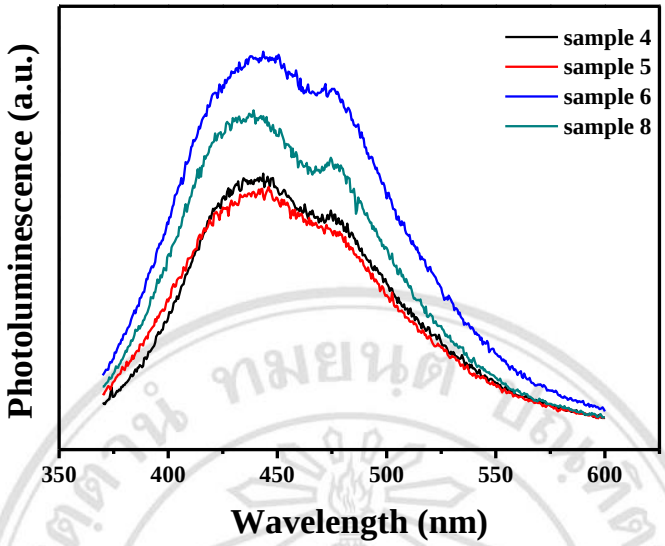

Figure 3.34 Photoluminescence spectra of CMC-$AgInS_2$ QDs synthesized by hydrothermal method excited by 350 nm.

The photoluminescence (PL) spectra of the CMC-$AgInS_2$ QDs excited by 350 nm wavelength at room temperature are shown in Figure 3.34. The emission spectra of 350 nm excitation wavelength corresponded with the Gaussian curve and showed the emission peak at about 440 nm, in accordance with the previous reports [9]. The PL spectra of CMC-$AgInS_2$ QDs have asymmetric peaks and broad peaks with a FWHM larger than 150 nm. This is normally observed and ascribed to the defect on CMC-$AgInS_2$ QDs and donor-acceptor transition in nanoscale ternary semiconductors. The asymmetric PL peaks observed to the defect-induced emission in CMC-$AgInS_2$ QDs. The PL peaks consist of two Gaussian peaks. The peak on the blue side is referred to as Peak 1, while the other one is Peak 2. The peak 1 occurred surface defect and the peak 2 is from internal defect. The photoinduced processes observed in the Figure 3.35. The intensity of emission peaks depend on defect and the ratio of precursors [57, 58].

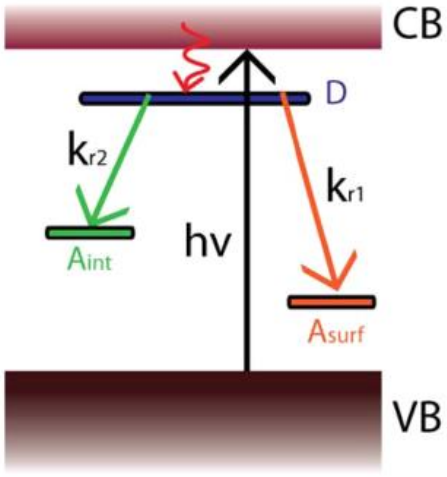

Figure 3.35 The photoinduced processed in ternary QDs: D is donor site, A_{int} and A_{surf} are acceptor sites for internal and surface defect, respectively [58].

The emission wavelength and color of the sample dependent on the size and composition of the sample (QDs). The QDs can be designed the emission wavelength. Concentration of silver nitrate and difference of sulfur sources affect properties of CMC-$AgInS_2$ QDs. The emission spectra of CMC-$AgInS_2$ QDs were influenced by the particle sizes. The larger distribution of nanocrystallite size can cause broadening of PL peak [1, 59].

3.2 Drug Encapsulation Studies

Synthesizing nanoparticles drug carrier systems has always been complicated by designing an appropriate size to carry effective drug payload and ability to target to right place. Identification of physicochemical parameter are absolutely critical in determining the particle interaction within a biological environment, aggregation tendencies, adsorption of protein in nanoparticle surface and intracellular trafficking of nanoparticles. A substantial variation in any of these factors can contribute to poor drug delivery, loss of therapeutic efficiency, and/or toxicity. Thus, the efficacytoxicity balance of nanoparticle system largely depends on their physicochemical properties. The ideal nanoparticle for derivering conventional therapeutics to cancer cells is less than 200 nm in size with a spherical shape and a smooth texture in order to easily transport through cancer vasculature in into cancer cells [60]. Therefore, The CMC-$AgInS_2$ QDs (sample 8) was used appropriate for biomedical application.

The development of nanocarrier for drug delivery, surface of nanoparticle must have functional groups that can conjugate with drug molecules. Herein, as mentioned above, the surface of $AgInS_2$ QDs was successfully coated with carboxymethyl cellulose.

It is known that the CMC is negatively charged polysaccharide (mainly due to carboxylic groups) which can be conjugated with positively charged drug e.g. doxorubicin (DOX) *via* electrostatic interaction. Furthermore, this conjugate demonstrated pH-triggered drug release behavior [23]. Practically, QD with spherical shape is an ideal for drug delivery application. Thus, in this application, sample 8 was used to study [60].

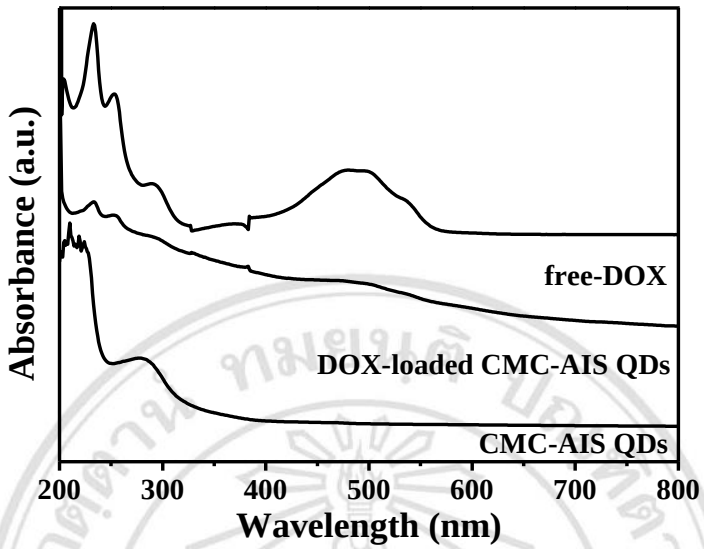

Figure 3.36 Absorbance spectra of the PBS solutions containing free-DOX, CMC-$AgInS_2$ QDs and DOX-loaded CMC-$AgInS_2$ QDs.

The characteristic absorbance of the drug DOX was at 480 nm that can be clearly seen in the absorption spectrum of the composite nanoparticle. The absorption spectra of CMC-$AgInS_2$ QDs had two peaks at 210 and 280 nm. The conjugation of CMC-$AgInS_2$ QDs and encapsulation of DOX in carboxymethyl cellulose has resulted in the broad absorption peak in the spectra of DOX-loaded CMC-$AgInS_2$ QDs. These results were in consistence with the previous report [22]. This indicates the success of DOX conjugation on CMC-$AgInS_2$ QDs.

Polymer–drug conjugate consists of a hydrophilic polymer carriers bearing in its side chains drug moieties and the spacer group by chemical conjugation or physical entrapment have been attempted. CMC has a negative charge polysaccharide. This negatively charged CMC can then be attracted with the positively charged drugs such as doxorubicin (DOX) *via* electrostatic interaction [23].

For loading of DOX, CMC-$AgInS_2$ QDs was first dissolved in PBS solution. The carboxyl group of CMC were changed to carboxylate groups. The ammonium cation of DOX were changed to amino groups. Then DOX-loaded CMC-$AgInS_2$ QDs synthesized *via* electrostatic interaction between the amino groups of doxorubicin (DOX) and carboxyl group of carboxymethyl cellulose sodium salt (CMC) [23, 61].

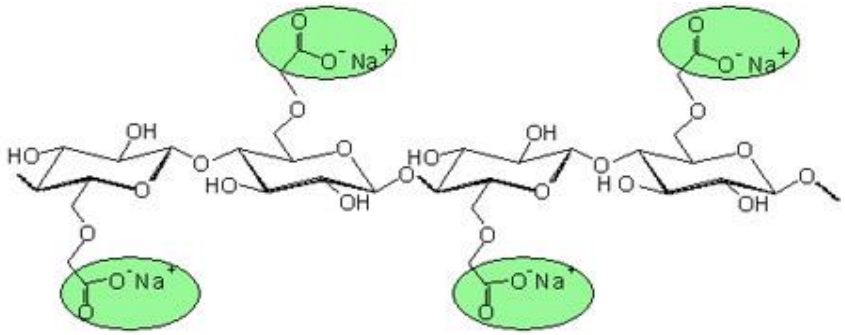

Figure 3.37 The structure of carboxymethyl cellulose sodium salt (CMC) [62].

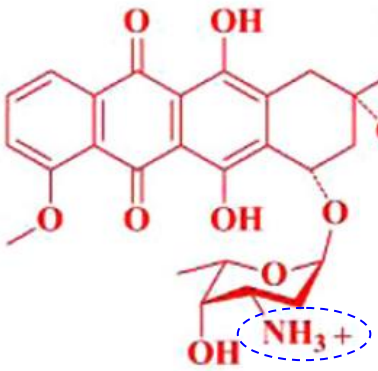

Figure 3.38 The structure of doxorubicin (DOX) [61].

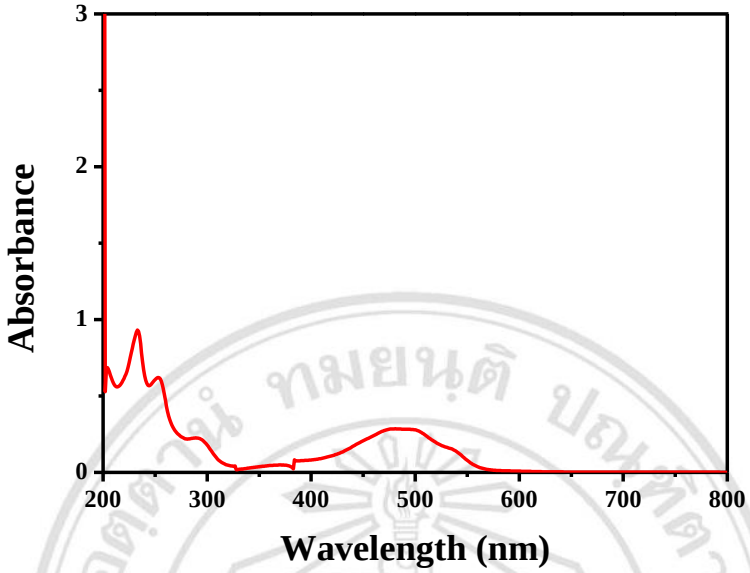

Figure 3.39 Absorbance spectrum of the PBS solutions containing free-DOX (supernatant).

Qualitative analysis on drug conjugation was carried out by measuring the absorbance of free-DOX and free DOX (supernatant) as shown in Figure 3.39. From the studies conducted on DOX entrapping efficiency (%DEE) and DOX loading efficiency (%DLE), it was found that the percentages of the DEE and the DLE were determined to be 50% and 14%, respectively.

3.3 Cellular Uptake of CMC-$AgInS_2$ QDs

Cellular uptake in a human breast cancer cell line (MCF7 cells). cellular uptake of DOX-loaded CMC-$AgInS_2$ QDs was studied by flow cytometry and Fluorescence microscopy. Flow cytometry was performed to study the behavior of DOX-loaded CMC-$AgInS_2$ QDs for targeting to MCF7 cells.

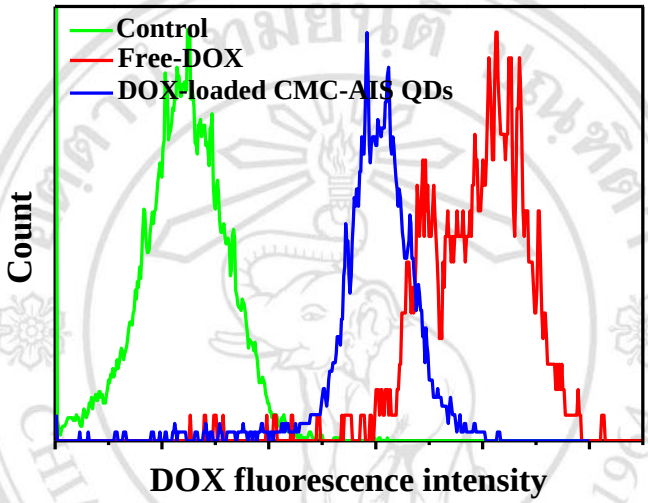

Figure 3.40 Cellular drug uptake analysis by using flow cytometer of control cell and the cells treated with free DOX and DOX-loaded CMC-$AgInS_2$ QDs.

The fluorescence signal observed in DOX-loaded CMC-$AgInS_2$ QDs treated cells (as observed by flow cytometry, Figure 3.40) was lower than that observed in the DOX treated cells. This may be due to the different cellular uptake pathways between free DOX (diffusion) and DOX loaded (endocytosis), leading to the difference on uptake kinetic between both systems [63].

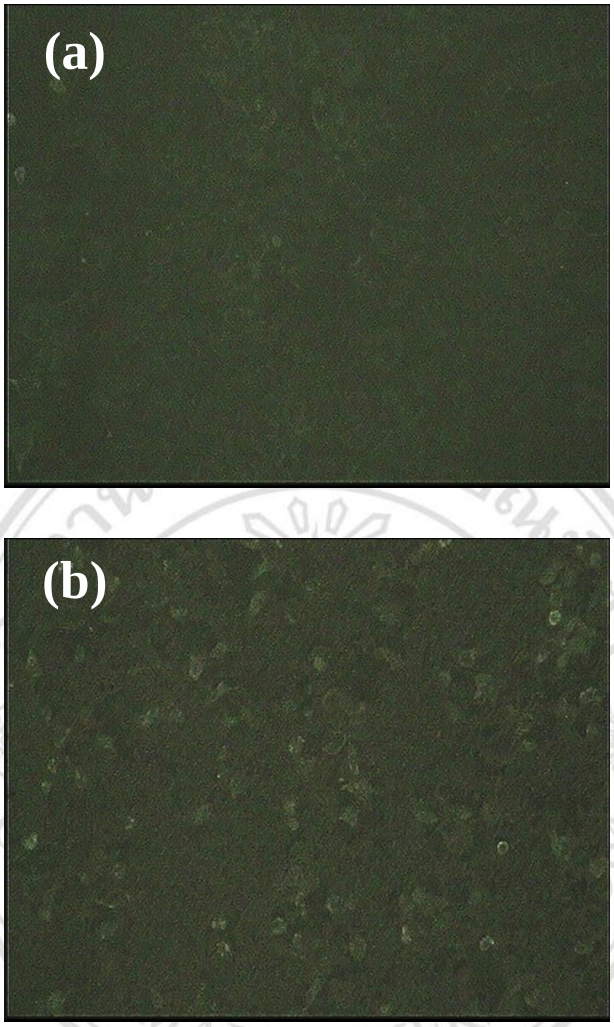

Figure 3.41 Fluorescence microscope images of MCF7 cells incubated with (a) control cells and (b) CMC-$AgInS_2$ QDs.

The internalization of DOX-loaded CMC-$AgInS_2$ QDs by MCF7 cells was also studied by the fluorescence images. The nanoparticles were internalized via the carbohydrate receptor present in the cancer cells that were observed by the fluorescence emitted by the DOX-loaded CMC-$AgInS_2$ QDs.

Because of fluorescence property of CMC-$AgInS_2$ QDs (450 – 550 nm), their intracellular uptake can be observed *via* its green fluorescence. As shown in Figure 3.41, a higher relative cellular fluorescent intensity was observed in the cells treated with CMC-$AgInS_2$ QDs, as compared with autofluorescence in the untreated cells.

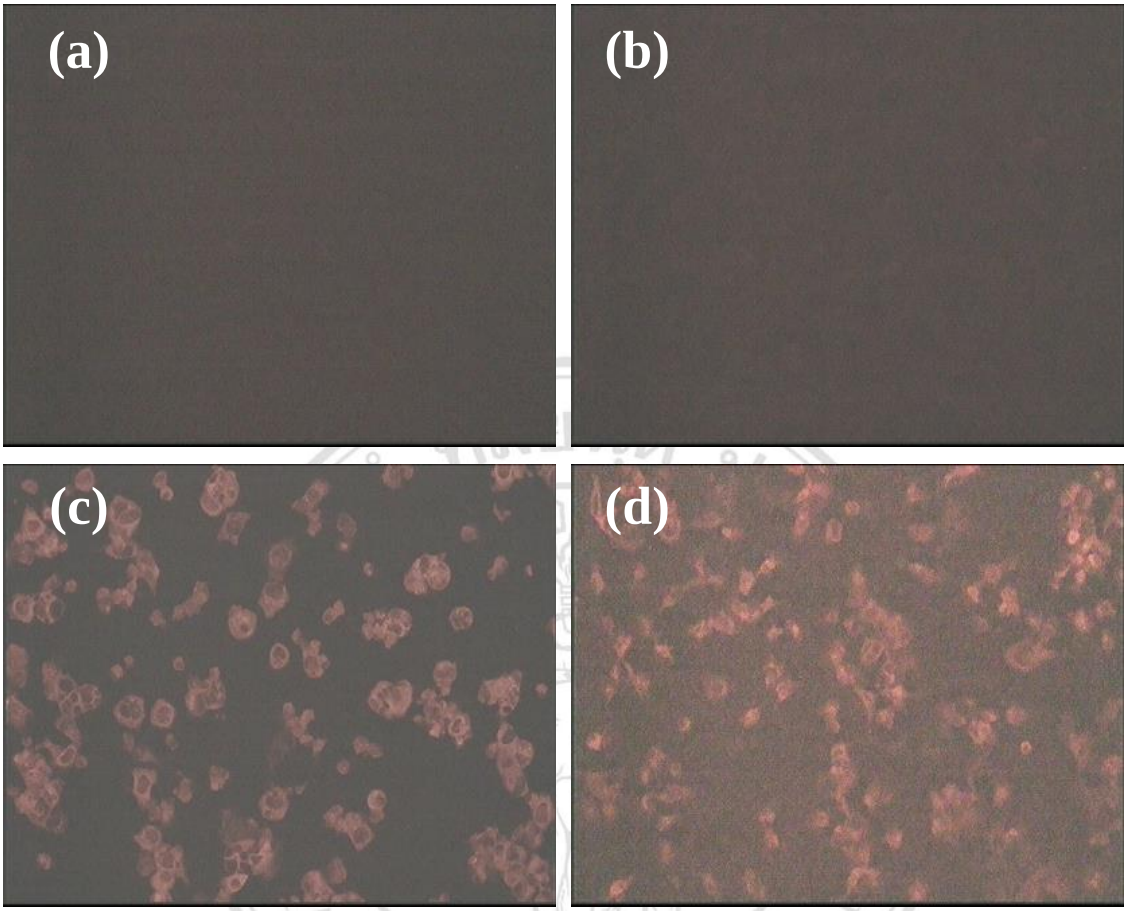

Figure 3.42 Fluorescence microscope images of (a) control cells and the cells treated with (b) CMC-$AgInS_2$ QDs, (c) free DOX and (d) DOX-loaded CMC-$AgInS_2$ QDs for 5 h.

This confirmed that CMC-$AgInS_2$ QDs can enter and uptake inside the cells. As a result, it can be concluded that the presence of CMC on surface of the QDs not only improves water dispersibility of QDs but may also enhance QD uptake by the cells *via* carbohydrate receptor-mediated endocytosis [64, 65].

To show the feasibility of CMC-$AgInS_2$ QDs as nanocarrier, intracellular uptake of DOX-loaded CMC-$AgInS_2$ QDs and free DOX was also observed *via* intrinsic red fluorescence of doxorubicin. Figure 3.42 shows fluorescence microscope images of the cells treated with different samples. It was found that DOX fluorescence was not only observed in the cells treated with free DOX but also DOX-loaded CMC-$AgInS_2$ QDs, indicating efficient delivery of drug molecules by CMC-$AgInS_2$ QDs. By contrast, such

fluorescence signal was not detected in control cells (without QDs) and CMC-$AgInS_2$ QDs treated cells.

When the MCF7 cells were incubated with free DOX, CMC-$AgInS_2$ QDs and DOX-loaded CMC-$AgInS_2$ QDs, red fluorescence of DOX was found to localize in the MCF7 and green fluorescence of CMC-$AgInS_2$ QDs. CMC-$AgInS_2$ QDs weak fluorescence was observed in MCF7 cells. Therefore the MCF7 cells were incubated with DOX-loaded CMC-$AgInS_2$ QDs was observed red fluorescence of DOX-loaded CMC-$AgInS_2$ QDs. If the release DOX to cells, green fluorescence of CMC-$AgInS_2$ QDs was observed in cells.

3.4 Biocompatibility Studies

The biocompatibility of CMC-$AgInS_2$ QDs was studied with MCF7 cells by MTT assay.

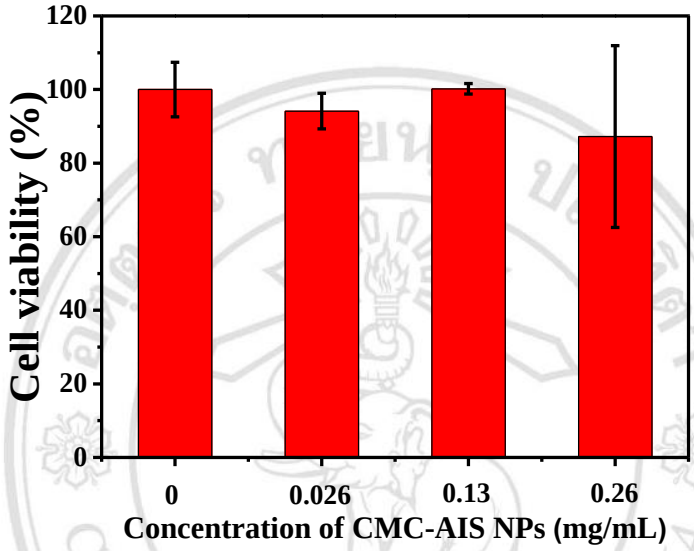

Figure 3.43 Biocompatible of CMC-$AgInS_2$ QDs synthesized by hydrothermal.

The biocompatibility of CMC-$AgInS_2$ QDs was proved by the viability of 87 % with MCF7 in MTT assay at high concentration of CMC-$AgInS_2$ QDs (0.26 mg/ml). As shown in Figure 3.43, no significant reduction on cell viability was observed in the cells treated with different amounts of CMC-$AgInS_2$ QDs, indicating good biocompatibility of this QD.

3.5 Cytotoxicity Studies

The cytotoxicity of free DOX and DOX-loaded CMC-$AgInS_2$ QDs was studied with MCF7 assay.

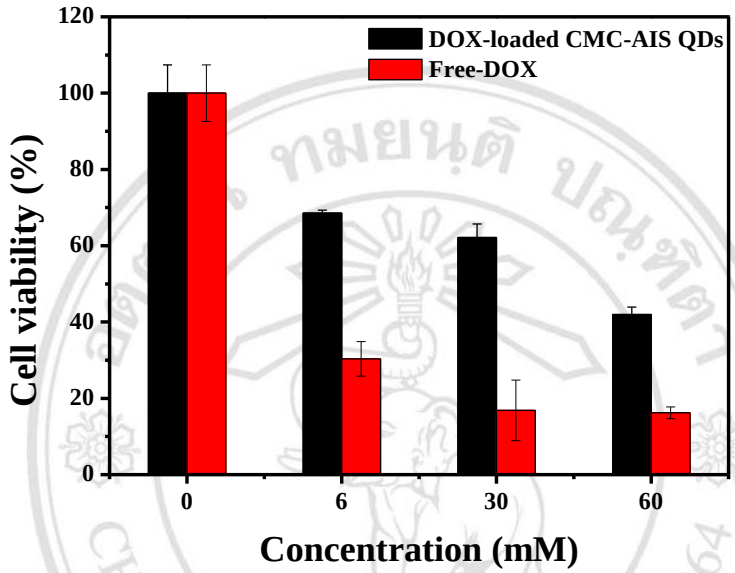

Figure 3.44 Cytotoxicity of the free DOX and DOX-loaded CMC-$AgInS_2$ QDs against MCF7 cells after being treated for 48 h.

As shown in Figure 3.44, as DOX concentration was increased, the cell viability decreased. Unfortunately, the toxicity of DOX-loaded CMC-$AgInS_2$ QDs was lower than that observed in free DOX. This may be due to the different modes of cellular uptake and internalization between two systems in order to exert their toxicity. It is well known that free DOX can enter into the cells by diffusion process, while the QDs can enter and accumulate inside the cells via receptor-mediated endocytosis process [66-68]. These two different mechanisms lead to the difference of cellular pharmacodynamics of drug molecule in order to exert its toxicity [69].

However, the advantages for using CMC-$AgInS_2$ QDs as nanocarrier include simplicity of drug loading and a potential candidate of CMC as cancer-specific molecule. Thus, CMC-$AgInS_2$ QDs could be a new nanoplatform for cancer treatment.